HHS Public Access

Author manuscript

Phys Med Biol. Author manuscript; available in PMC 2024 July 24.

Published in final edited form as:

Phys Med Biol. ; 68(15): . doi:10.1088/1361-6560/ace0f0.

Unsupervised deep learning-based displacement estimation for vascular elasticity imaging applications

Grigorios M. Karageorgos[1], **Pengcheng Liang**[1], **Nima Mobadersany**[2], **Parth Gami**[1], **Elisa E. Konofagou**[1]

[1]Biomedical Engineering Department, Columbia University, New York, NY, USA

[2]Department of Radiology, Columbia University, New York, NY, USA

Abstract

Objective: Arterial wall stiffness can provide valuable information on the proper function of the cardiovascular system. Ultrasound elasticity imaging techniques have shown great promise as a low-cost and non-invasive tool to enable localized maps of arterial wall stiffness. Such techniques rely upon motion detection algorithms that provide arterial wall displacement estimation.

Approach: In this study, we propose an unsupervised deep learning-based approach, originally proposed for image registration, in order to enable improved quality arterial wall displacement estimation at high temporal and spatial resolutions. The performance of the proposed network was assessed through phantom experiments, where various models were trained by using ultrasound RF signals, or B-mode images, as well as different loss functions.

Main results: Using the mean square error (MSE) for the training process provided the highest signal-to-noise ratio when training on the B-modes images (30.36±1.14 dB) and highest contrast-to-noise ratio when training on the RF signals (32.84±1.89 dB). In addition, training the model on RF signals demonstrated the capability of providing accurate localized pulse wave velocity (PWV) maps, with a mean relative error (MRE_{PWV}) of 3.32±1.80 % and an R2 of 0.97±0.03. Finally, the developed model was tested in human common carotid arteries in-vivo, providing accurate tracking of the distension pulse wave propagation, with an MRE_{PWV}=3.86±2.69 % and R2=0.95 ± 0.03.

Significance: In conclusion, a novel displacement estimation approach was presented, showing promise in improving vascular elasticity imaging techniques.

Keywords

Arterial wall displacement; vascular elasticity imaging; deep learning; neural network; carotid artery disease

1. Introduction

Large artery stiffness has been widely considered as a key parameter in cardiovascular disease progression. Stiffening of the arterial wall reflects the process of structural

* gk2490@columbia.edu; ek2191@Columbia.edu.

alterations due to the loss of elastin, and cumulation of collagen fibers [1][2][3]. These structural alterations are closely related with vascular ageing and chronic hypertension, which can potentially damage the circulatory system, leading to cardiovascular events such as heart attack and stroke[2][4][5][6].

Changes in large artery mechanics have also been associated with focal vascular diseases such as carotid atherosclerosis. This condition involves formation of atherosclerotic plaques in the carotid artery wall, obstructing blood flow to the brain. In case of atherosclerotic plaque rupture, a blood clot may form and transfer to the cerebral vasculature, causing an ischemic stroke [7]. Pre-clinical stages of carotid atherosclerosis have been associated with increased wall stiffness and inhomogeneous arterial mechanical properties [8][9]. In addition, the stiffness of an atherosclerotic plaque can provide information on its structural components, and risk for rupture [10][11].

Ultrasound elasticity imaging techniques have shown great promise as a low-cost, non-ionizing and non-invasive tool to provide reliable, localized maps of arterial wall stiffness. Vascular elastography methods have shown capability of characterizing the mechanical properties of the arterial wall, as well as atherosclerotic lesions, by imaging physiologically induced arterial strain [12][13][14][15][16]. Acoustic Radiation Force Imaging (ARFI) is another approach that applies acoustic radiation force to deform the examined tissue, and then measure the resulting deformation. Application of this technique demonstrated the feasibility to differentiate between stable and unstable plaque features, validated with histological examination of human plaque samples [10]. In addition, Shear Wave Elastography (SWE) has been widely utilized for arterial wall and plaque stiffness characterization, which estimates tissue elasticity by tracking the ARFI induced shear wave propagation [17][18][19].

Pulse Wave Velocity (PWV) is a well-established index of arterial stiffness that has been linked with all-cause cardiovascular morbidity and mortality [20][21]. Pulse Wave Imaging (PWI) [22][23][24][25][26][27][28] is an ultrasound elasticity imaging technique that enables localized maps of PWV, by tracking the propagation of the distension Pulse Wave (PW) along an imaged arterial segment. In turn, PWV can be associated, under specific assumptions, to the Young's modulus and compliance of the imaged vessel, through the Moens-Korteweg and Bramwell-Hill equations, respectively. PWI has shown great promise in diagnosis and monitoring of cardiovascular conditions such as hypertension and atherosclerosis [29][30][31][32][33][34].

The aforementioned ultrasound elasticity techniques rely upon motion tracking algorithms, in order to image the displacements of the imaged tissue and derive elasticity maps. The most commonly used algorithm involves matching 1-D or 2-D kernels among consecutive temporal ultrasound RF frames, B-mode images, or spectrograms [23][35][36][37][38]. In particular, a reference kernel is defined in a temporal frame, and then compared with candidate kernels, within a pre-determined search-range, in subsequent frames. A cost function, typically the normalized cross-correlation is evaluated to quantify the similarity between kernels. The displacement is derived through the spatial and temporal shift between the reference and the best matching kernels. This approach has been the basis of the

majority of ultrasound elasticity imaging techniques. However, it entails limitations, such as dependency of displacement maps on the kernel size and the search range, as well as the rigid shift of the kernel that may ignore complex displacement patterns. In addition, the kernel matching technique estimates the displacement of the reference kernel, rather than each pixel in the image, which deteriorates the spatial resolution of the displacement maps.

Tissue Doppler Imaging (TDI) is a displacement estimation method that has been utilized for arterial elasticity imaging [39][40][41][42]. According to this approach, the autocorrelation function is applied on the received RF signals, in order to estimate the phase shift induced through moving scatterers. However, TDI is highly dependent on the beam-to-flow angle, it is more sensitive to noise, while also a high frame rate is required in order to avoid aliasing [43].

Recently, deep learning-based techniques have been investigated for tissue displacement estimation. The aim of those techniques is to train models that will learn the displacement patterns in ultrasound acquisition sequences. Several approaches have been based on the well-known PWC-Net architecture [44][45][46], demonstrating the feasibility to provide strain maps in simulated ultrasound data [45], breast phantoms and liver cancer patients [46]. The main limitation of those techniques involved high degree of variance in the displacement maps compared to conventional methods, due to the lack of a regularization factor. In addition, a deep-learning-based approach for ARFI imaging has been proposed [47]. The latter displacement estimation model was trained on synthetic data and tested both in phantom and in-vivo prostate ARFI data. Moreover, a Siamese neural network scheme has been employed to estimate the motion of the carotid artery in simulations and experimental data [48]. However, the presented approach limited the displacement estimation in single point target in the field of view and did not provide complete information on the spatiotemporal variation of the imaged arterial segment.

The aforementioned techniques mainly use supervised learning, i.e., the models are trained with known ground-truth displacement maps [45][47]. This fact limits the training process on simulation and/or experimental data, which in turn may limit the capability of the model to generalize in more complex in-vivo acquisitions. To address such limitations, semi-supervised [49] and unsupervised [50][51] deep learning approaches have been developed, focusing mainly on strain elastography applications. In [50][51], a U-net, combined with long-short-term memory units (LSTM) was trained using pairs of ultrasound temporal frames for quasi-static elastography, in simulated data and in-vivo acquisitions of the arm in healthy volunteers. A regularization factor was included in the loss function to limit the variance in the displacement maps. Additional studies have applied unsupervised learning to estimate the myocardial motion in canine models in vivo [52][53].

Deep learning has shown great promise in providing accurate displacement maps for various ultrasound elasticity imaging applications. However, the capability of unsupervised deep learning to reconstruct high spatial and temporal resolution arterial wall displacements, induced by the distension pulse wave propagation, has not yet been investigated. In the study presented herein, we propose an unsupervised deep learning approach for arterial wall displacement estimation. The Voxelmorph [54], a neural network for image registration is

trained on high frame rate ultrasound RF and B-mode sequences, in order to learn arterial wall motion patterns. The performance of the deep-learning based displacement estimator is assessed through vessel phantom experiments in terms of elastographic contrast and signal to noise ratio. In addition, the feasibility of the proposed technique to track the propagation of the distension pulse wave is evaluated in the same vessel phantom setup, and human common carotid arteries in vivo.

2. Methods

2.1 Ultrasound acquisition setup

A Verasonics Vantage 256 research platform (Verasonics, Bothell, WA, USA) was equipped with an L7-4 Linear array transducer with 128 elements, center frequency 5 MHz and 50% Bandwidth (L7-4, ATL Ultrasound, Bothell, WA, USA). A 3-or 5-plane wave compounding acquisition imaging sequence was implemented at transmit angles of either (1°,0°,1°,), or (−2°,−1°,0°,1°,2°). A pulse repetition frequency within a range of 9500-10000 Hz was used, depending on the depth of each imaged vessel. RF signals were recorded for a time interval of 1 s per ultrasound acquisition.

2.2 Phantom Study

Phantom experiments were carried out in two vessel phantoms of different stiffness values, similarly as in [55][56][57], to assess the performance of the proposed deep learning-based displacement estimator (Figure 1). A polyvinyl alcohol (PVA) mixture was formed by mixing distilled water, PVA powder (Sigma-Aldrich, St. Louis, MO, USA), glycerol and graphite acoustic scatterers (Sigma-Aldrich, St. Louis, MO, USA) at concentrations of 78%, 10%, 10% and 3%, respectively. The mixture was initially heated at 90 °C for approximately 40 minutes. Subsequently, the mixture was thawed and poured inside two separate cylindrical molds. The two molds were subjected to six, and three cycles of freezing (12 h at −20 °C) and thawing (12 h at room temperature), respectively, resulting in two vessel phantoms with different wall stiffness. The former phantom (training/validation phantom) was used to obtain the training/validation dataset, while the latter (test phantom) was used to test the generalization capability of the model in a vessel with different wall stiffness.

The resulting elastic phantoms were fixed inside two separate plastic containers, which were in turn filled with porcine-skin gelatin (Sigma-Aldrich, St. Louis, MO, USA), to serve as the surrounding medium. The open ends of the phantoms were attached onto plastic fittings, which were connected to a programmable physiological flow pump (Compuflow 1000, Shelley Medical Imaging technologies, Ontario, Canada). A pulsatile flow waveform was applied in the phantom lumen, with an amplitude of 10 mL/s and a frequency of 0.53 Hz.

The plastic containers were filled with water, and the ultrasound transducer was attached to a positioner in order to perform ultrasound scans. N=18, and N=5 acquisitions were carried out in the training/validation and test phantoms, respectively, capturing 2-D longitudinal images at different locations across the phantoms' axis. A training/validation split of 13/5 acquisitions was carried out in the case of the former phantom.

2.3 In vivo study

All procedures pertinent to the human study were approved by the Human Research Protection Office (HRPO) and Institutional Review Boards (IRBs) of Columbia University (protocol AAAR0022). The left and right common carotid arteries of N=10 human subjects with no prior history of cardiovascular disease were scanned in vivo. (6 Male, 4 Female; 28.7 ± 4.1 y.o.), resulting in a total of 20 ultrasound acquisitions. A training/validation split of 7/3 subjects, corresponding to 14/6 acquisitions, was carried out for the in-vivo study.

2.4 Data pre-processing & training dataset

Data pre-processing was carried out in MATLAB 2017b (MathWorks Inc, Natick, MA, USA). The acquired RF signals were beamformed by employing a GPU-accelerated implementation of the delay and sum algorithm, by using the respective transmission angle on receive for each frame. The beamformed RF frames were coherently summed for each set of 5 transmission angles, producing thus compounded RF frames of improved quality [58]. The F-number used in the beamforming process was 1.7, and apodization on receive was implemented using a Hanning filter. The axial and lateral resolution of the beamforming grid was 0.01848 mm and 0.2980 mm, respectively. The frame rate of the resulting image sequence after compounding was equal to approximately 1900-2000 Hz. Subsequently, the envelope of the compounded RF frames was extracted through the Hilbert transform and the output was log-compressed in order to obtain a sequence of B-mode images.

Two separate datasets were formed, by using the compounded RF frames, or the B-mode images. Both in the in-vivo and phantom acquisitions, N=13 acquisitions were used as the training dataset. Temporal frames ($I_{t_n}(x_i, y_j) = I_{t_n}$) in the training dataset were normalized within a range of [0 1], and were resized to 128 samples across the lateral direction (x_i) and 768 samples across the axial direction (y_j). Each frame, I_{t_n}, was paired with its subsequent frame $I_{t_{n+1}}$, resulting in a total of 24,950 pairs for the training dataset.

2.5 Deep learning-based displacement estimator

The aim is to train a neural network in an unsupervised fashion, in order to learn the displacement patterns of a moving object in high frame rate ultrasound image sequences. The developed technique is based on the Voxelmorph, a deep learning approach originally used to register MRI images of the brain [54]. A pair of consecutive ultrasound temporal frames ($I_{t_n}(x_i, y_j) = I_{t_n}, I_{t_n+1}(x_i, y_j) = I_{t_n+1}$) are concatenated into a 2-channel 2-D image. The symbols x_i, y_j, ($i \in [1\ 128]$, $j \in [1\ 768]$), stand for the lateral and axial positions, respectively. The concatenated image is provided as an input to a U-net, which performs spatial transformations through an encoding, followed by a decoding stage. The output of the U-net is a 2-D Displacement field $\left(\overrightarrow{D}(x_i, y_j) = \overrightarrow{D}\right)$, depicting the relative displacement of each pixel in frame I_{t_n+1}, with respect to frame I_{t_n}.

2.5.1 Model architecture—The model architecture is depicted in Figure 2. Each layer in the encoding stage of the U-net [59] consists of a convolutional layer, characterized by either 16, or 32 filters of size 3x3 and stride of 1. Subsequently, a ReLU activation function

with a parameter 0.2 is applied, followed by a max pooling operator of size 2x2. Each layer in the encoding stage down-samples the output of the previous layer to ½ of its size, and extracts progressively higher-level features of the input used to learn the Displacement field, $\overrightarrow{D}$ [54].

In the decoding stage, each layer applies a convolution operator, consisting of 32 filters of size 3x3 and stride of 1. The output of the convolution is in turn up-sampled, by a factor of 2, in order to obtain the original size of the input volume (I_{t_n}, $I_{t_{n+1}}$). Skip connections are used that concatenate the output features of each layer in the decoder with the features of the respective layer in the encoding stage. The skip connections propagate fine-grained details learned in the encoding stages, in order to enable precise spatial registration during image reconstruction in the decoding part [59]. Following the decoding stage, additional convolutional layers are applied to refine the decoded image and produce the displacement map, $\overline{D}$ [54].

2.5.2 Model training—The training process is described in Figure 3. Let T() denote the spatial transformation operator that displaces each pixel in $I_{t_{n+1}}$ with respect to $\overrightarrow{D}$, in order to provide an approximation of I_{t_n}:

$$\widehat{I_{t_n}} = T\left(I_{t_{n+1}}, \overrightarrow{D}\right) = I_{t_{n+1}}\left((x_i, y_j) + \overrightarrow{D}(x_i, y_j)\right) \quad (1)$$

T() was implemented similarly as in [54]. The aim is to provide an optimal displacement field $\overrightarrow{D}(x_i, y_j)$, that will accurately depict the relative displacement of each pixel in $I_{t_{n+1}}$, with respect to I_{t_n}. This is equivalent to maximizing the similarity between $\widehat{I_{t_n}}$ and I_{t_n}. Therefore, the described neural network is optimized based on an unsupervised loss function ($L_{sim}()$) that penalizes differences between $\widehat{I_{t_n}}$ and I_{t_n}.

Optimizing based solely on the similarity loss function, may entail spatial discontinuities in the resulting displacement field, that do not correspond to realistic physiological arterial wall motion. In order to encourage spatial continuity in the displacement maps across the arterial walls, a regularization factor is also added ($L_{reg}()$), which penalizes variations in the spatial gradient of $\overline{D}$ [54]:

$$L_{reg}\left(\overrightarrow{D}\right) = \sum_{i=1}^{N_x} \sum_{j=1}^{N_y} \left\| \overrightarrow{\nabla} \overrightarrow{D}(x_i, y_j) \right\|^2 \quad (2)$$

Therefore, the total loss function ($L_{tot}()$) is calculated as:

$$L_{tot}\left(\widehat{I_{t_n}}, I_{t_n}, \overrightarrow{D}\right) = L_{sim}\left(\widehat{I_{t_n}}, I_{t_n}\right) + \lambda L_{reg}\left(\overrightarrow{D}\right) \quad (3)$$

where λ is a constant that determines the contribution of $L_{reg}()$ in the total loss function, and was set equal to 0.05 [54].

Two different functions were used as $L_{sim}()$ to train the model:

- The mean squared error, MSE:

$$MSE\left(\widehat{I_{t_n}}, I_{t_n}\right) = \frac{1}{N_x N_y} \sum_{i=1}^{N_x} \sum_{j=1}^{Ny} \left| T\left(I_{t_{n+1}}, \overrightarrow{D}\right) - I_{t_n} \right|^2 \quad (4)$$

- The local normalized cross-correlation, NCC. Given a small region in the image, **v**, consisting of n pixels $\{v_1, v_2, \ldots, v_n\}$, the employed NCC function is given by the following formula:

$$NCC\left(\widehat{I_{t_n}}, I_{t_n}\right) = \sum_{v \in I_{t_n}} \frac{\sum_{i=1}^{n} \left(\left(I_{t_n}(v_i) - \overline{I_{t_n}(\mathbf{v})}\right) * \left(T\left(I_{t_{n+1}}, \overrightarrow{D}\right)(v_i) - \overline{T\left(I_{t_{n+1}}, \overrightarrow{D}\right)(v)}\right)\right)^2}{\sum_{i=1}^{n} \left(I_{t_n}(v_i) - \overline{I_{t_n}(\mathbf{v})}\right)^2 * \sum_{i=1}^{n} \left(T\left(I_{t_{n+1}}, \overrightarrow{D}\right)(v_i) - \overline{T\left(I_{t_{n+1}}, \overrightarrow{D}\right)(v)}\right)^2} \quad (5)$$

where $\overline{I_{t_n}(\mathbf{v})}$ denotes the local mean intensity of pixels within a volume v, and n was set equal to 9. This version of NCC() has been reported to serve as a more robust marker of image similarity index. More detailed description of this metric can be found in [60].

For each loss function, two different models were trained by using the RF signals, or the B-mode images. Thus, a total of four models were trained separately for the phantom and in vivo acquisitions: (**RF-MSE**: training on RF signals using MSE loss, **RF-NCC**: training on RF signals using NCC loss, **Bm-MSE**: training on B-modes using MSE loss, **Bm-NCC**: training on B-modes using NCC loss). The same training dataset, consisting of 24,950 pairs was employed for each model.

The model was trained by using the ADAM optimizer, with a learning rate of 10^{-4}, over 100 epochs. Mini-batch stochastic gradient descent was employed, with a batch size of 20, resulting in 1248 steps per epoch. Early stopping regularization was also used, with a patience of 7 epochs, in order to avoid overfit. All models were based on the Voxelmorph Keras [61] implementation described in [54], enabled by Tensorflow [62] version 2.3. Training was carried out on an Nvidia Quadro P6000 graphics processing unit (GPU) (Nvidia, Santa clara, California, USA).

2.6 Displacement performance assessment

Displacement performance assessment was carried out in terms of elastographic signal-to-noise and contrast-to-noise ratio, as well as accuracy in distension pulse wave tracking. In the case of the phantom study, the 5 validation acquisitions in the training/validation phantom were used to evaluate the quality and accuracy of the displacements, based on which the best performing model was selected. The same model was inferred on the 5 acquisitions of the test phantom with different stiffness to assess its generalization capabilities. The in-vivo model was trained separately on the human subject acquisitions

by using the same training parameters and loss function as the best performing model determined through the phantom study.

Given the restricted lateral resolution provided by the employed ultrasound setup, and the motion of the artery along the axial direction, performance assessment was performed using only the wall axial displacements.

2.6.1 Signal and contrast-to-noise ratio—In the case of the phantom validation dataset, the quality of each displacement estimator was evaluated in terms of elastographic signal-to-noise (SNR_e) and contrast to noise (CNR_e) ratio.

Given the parallel orientation of the probe with respect to the phantom's axis and the axial motion of the wall, it can be hypothesized that the axial wall velocities are uniform within small axial regions of the phantom wall, $y_j \in [y_{wall}, y_{wall} + d]$. The symbols y_{wall}, d denote the position of the proximal wall derived through manual segmentation, and d a small distance which was fixed at 0.6 mm based on the physiological range of arterial wall media thickness values [63]. Based on this hypothesis, the elastographic signal to noise ratio at a given lateral position, x_i, and time frame, t_n, can be derived as follows:

$$SNR_e(x_i, t_n) = \frac{AVG_{y_j}\{v(x_i, y_j, t_n)\}|_{y_j \in [y_{wall}, y_{wall} + y_d]}}{STD_{y_j}\{v(x_i, y_j, t_n)\}|_{y_j \in [y_{wall}, y_{wall} + y_d]}} \quad (6)$$

Where $AVG_{y_j}\{\}$ and $STD_{y_j}\{\}$ denote the average and standard deviation operators across the y axis. A single SNR value was obtained, expressed in dB, by averaging $SNR_e(x_i, t_n)$ across all lateral positions ($x_i \in [0, x_{end}]$), at the peak systolic time frame (t_{PS}), as follows:

$$SNR_e(dB) = 20 \log_{10} AVG_{x_i}\left\{\frac{AVG_{y_j}\{v(x_i, y_j, t_{PS})\}|_{y_j \in [y_{wall}, y_{wall} + y_d]}}{STD_{y_j}\{v(x_i, y_j, t_{PS})\}|_{y_j \in [y_{wall}, y_{wall} + y_d}}\right\}\Bigg|_{x_i \in [0\ x_{end}]} \quad (7)$$

To calculate the elastographic contrast to noise ratio (CNR_e), a polygonal region on the proximal phantom wall was manually segmented by using the Matlab command roipoly() , as well as another region in the anechoic gelatin surrounding medium to serve as background, as shown in Figure 4. CNR_e was derived through the following formula [64]:

$$CNR_e(dB) = 20 \log_{10}\left\{2 * \frac{(AVG\{v_{tissue}\} - AVG\{v_{background}\})^2}{(STD\{v_{tissue}\})^2 + (STD\{v_{background}\})^2}\right\} \quad (8)$$

where v_{tissue} and $v_{background}$ denote the velocities in the regions of tissue and background, respectively.

The SNR_e and CNR_e were calculated for each acquisition and trained model. In addition, the same performance metrics were estimated for a conventional cross-correlation-based displacement estimator, to serve as reference. The employed conventional displacement estimation technique is described in [35], were a 1-D kernel is applied in a 2-D search to

estimate the inter-frame displacement field. A kernel size of 28 samples was used, with an overlap of 5% and a maximum search range of 4 axial samples. The displacement maps provided by the conventional displacement estimator were filtered in time by using a moving average window with a size of 10 temporal samples.

2.6.2 Distension pulse wave tracking—Given that the proposed technique is aimed for ultrasound elastography applications, it is important to determine whether it can accurately estimate tissue displacements throughout a given ultrasound imaging sequence. Therefore, instead of evaluating the accuracy in registration among individual pairs of temporal frames, it is more relevant to assess its capability to provide accurate maps of the spatiotemporal variation of arterial wall displacements.

An approach to derive such accuracy metrics is to carry out the Pulse Wave Imaging (PWI) technique for arterial stiffness characterization, which tracks the propagation of the distension pulse wave along an image arterial segment and provides a regional PWV estimate. The PWI processing methodology is depicted in Figure 5. The acquired ultrasound temporal frames are stacked together (Figure 5–A)), and fed to the U-net in pairs, in order to obtain the axial inter-frame displacements at each point location and time frame. The interframe displacements are normalized with the frame rate, and therefore are expressed in terms of axial velocities (Figure 5–B)). Subsequently, the proximal and distal walls are manually segmented (Figure 5–C)), in order to obtain the time waveforms of the axial wall velocities at each lateral position, x, of the proximal and distal walls ($v_{prox}(x_i, t_n)$, $v_{dist}(x_i, t_n)$), respectively). Subsequently the velocities of the distal wall are subtracted from the proximal wall, in order to obtain a spatiotemporal plot of the arterial wall distension (Figure 5–D)). Finally, a linear fit is applied on the time of occurrence of the 50% point among consecutive distension waveforms, versus the lateral position, x. The inverse of the slope of the fit yields a regional PWV estimate, while the coefficient of determination, R^2, of the linear fit yields the quality of pulse wave tracking.

The PWI processing methodology was carried out for each acquisition in the validation and test datasets. In each case, the relative error (MRE_{PWV}) between the PWV provided by the deep learning model (PWV_{DL}) and the reference PWV (PWV_{ref}) was calculated as follows:

$$MRE_{PWV} = 100 * \frac{PWV_{ref} - PWV_{DL}}{PWV_{ref}}\% \quad (9)$$

The PWV_{ref} was obtained by using the conventional PWI methodology reported in [58], which has been validated in multiple studies in phantoms and in-vivo. In addition, the R^2 was calculated as a performance metric, which quantifies how accurately the displacement estimator can reconstruct the phase shift of the distension pulse wave among different spatial positions.

3. Results

3.1 Phantom study

3.1.1 Signal and contrast to noise ratio—Figure 6–A) demonstrates an RF frame from the validation dataset. Figure 6–B),C) illustrate the 2-D axial velocity maps resulting from the model trained on RF frames by using the MSE (RF-MSE) and CC (RF-CC) loss functions, respectively. Figure 6–D) shows the B-mode image corresponding to the RF frame in Figure 6–A), while E),F) present the respective velocities using the model trained on the B-mode images (Bm-MSE, Bm-CC, respectively).

Using the MSE as a loss function (Figure 6–B),E)) provides more accurate delineation of the displacing walls, as compared to NCC (Figure 6–C),F)). On the other hand, it can be observed that NCC enhances weaker echoes originating from the blood mimicking fluid scatterers in the phantom lumen.

Figure 7–A),B) demonstrates the average and standard deviation of the SNR_e and CNR_e values, respectively, obtained by each trained model and the reference conventional displacement estimator (N=5 measurements per displacement estimation technique). It can be observed that the model trained using MSE, provided higher values for the quality metrics both in the case of RF and B-mode training, as compared to the reference technique, while the NCC loss function resulted in lower quality of tissue displacement estimation. The highest SNR_e was observed in the case of Bm-MSE (30.36±1.14 dB), followed by RF-MSE (27.12±1.01 dB). In the case of CNR_e, Bm-MSE provided higher performance (32.84±1.89 dB), as compared to BM-MSE (26.46±3.85 dB).

Comparison between the top two performing models was carried out by using an unpaired t-test. A significantly higher SNR_e was observed in the case Bm-MSE, as compared to RF-MSE (30.36±1.14 dB vs 27.12±1.01 dB, $p<0.01$), while the CNR_e was significantly lower for Bm-MSE, compared to RF-MSE (26.46±3.85 dB vs 32.84±1.89 dB, $p<0.05$).

3.1.2 Distension pulse wave tracking—Figure 7–C),D) illustrate the mean and standard deviation of MRE_{PWV} and R^2 (N=5), respectively, obtained by each trained model in the phantom validation acquisitions. The lowest MRE_{PWV} and highest R^2 (3.32 ± 1.80 %, 0.97 ± 0.03, respectively) were provided by the RF-MSE model, followed by Bm-MSE (10.27 ± 4.48 %, 0.95 ± 0.03, respectively). Models trained using NCC loss function did not provide displacements of adequate quality, in order to enable pulse wave tracking.

Figure 8–A),B),C) show three different time frames of the PWI image sequence derived through the RF-MSE model, where the axial wall velocities are color-coded and overlaid onto the B-mode image. The yellow arrow indicates the position of the wave-front of the pulse wave at each given time-frame. Figure 8–D,E) demonstrate the spatiotemporal map of arterial wall distension, as obtained through conventional PWI and RF-MSE, respectively, in one validation acquisition. Figure 8–F,G) illustrate the respective conventional PWI and RF-MSE spatiotemporal maps in one test acquisition. Excellent similarity can be observed between the spatiotemporal maps and PWV values, obtained through the different techniques.

Table I summarizes the PWV and R^2 values obtained using conventional PWI and the RF-MSE model in the 5 test acquisitions. The test MRE_{PWV} was equal to 3.92 ± 2.74 %, demonstrating the capability of the trained model to provide accurate displacement maps in data that were unseen during the training process.

3.2 In-vivo study

Figure 9 illustrates three examples of the in-vivo validation acquisitions. Figure 9–A),B),C) show the axial wall velocities, color-coded and overlaid onto the B-mode image. Sections D,E,F) and G),H),I) demonstrate the respective spatiotemporal maps, along with the estimated PWV and R^2 as obtained through conventional PWI and the RF-MSE model. It is noted that only the RF-MSE model was trained for the in-vivo data, given that it provided the most accurate pulse wave tracking in the phantom experiments (Section 3.1.2).

TABLE-II summarizes the PWV values and R^2, obtained through conventional PWI and RF-MSE, in each acquisition from the validation dataset. Good agreement was found between the PWV values measured with the two techniques, with a MRE_{PWV} = 3.86 ±2.69%. In addition, it can be observed that the R^2 was higher in the case of RF-MSE (0.95 ± 0.03) displacement estimator, compared to the conventional PWI (0.92 ± 0.04) suggesting that the proposed deep learning approach can potentially provide more robust spatiotemporal maps of arterial wall distension and pulse wave tracking.

4. Discussion

In the study presented herein, a deep-learning-based approach for arterial wall displacement estimation was presented. The Voxelmorph, a neural network for spatial image registration was trained on ultrasound images of the carotid artery, demonstrating the capability to provide high-quality pixel-to-pixel displacements of the arterial wall. Four different models were trained using either ultrasound RF frames or B-mode images, and two different loss functions. The performance of each trained model was assessed in vitro, in a straight vessel phantom. Finally, the feasibility of the proposed technique to track the distension pulse wave propagation was demonstrated in human common carotid arteries in-vivo.

The proposed technique performs pair-specific optimization, in order to derive the spatial transformation that depicts the displacement field between consecutive temporal ultrasound frames. This is achieved by minimizing appropriate loss functions that model the similarity between a given temporal frame, and a subsequent temporal frame displaced by the spatial transformation. Therefore, the model can learn arterial motion patterns without the need to use a-priori knowledge of ground-truth displacements, which would be rather challenging to obtain in-vivo. A regularization factor is added to the loss function that penalizes large spatial gradients in the displacement maps, in order to discourage discontinuities among different temporal frames that are not related to physiological arterial wall motion.

Using the MSE as a loss function for the training process out-performed NCC, as determined by the employed displacement quality and accuracy metrics. MSE was expected to provide higher quality tissue displacement estimates, given that it prioritizes high intensity pixels corresponding to bright echoes originating from the arterial walls. On the contrary,

NCC is less dependent on pixel intensity, and therefore prioritizes tracking of fast-moving scatterers present in the blood, over the slow-moving arterial tissue. This effect is apparent in Figures 6–C),F), where the NCC-based models track primarily the motion of the blood mimicking fluid. Therefore, NCC may be more relevant when training the model for blood flow imaging.

A potential advantage of the presented approach over conventional kernel matching displacement estimation methods is the fact that it does not require a-priori determination of hyperparameters such as the kernel size, kernel shift and search range, that significantly affect the performance of displacement estimation. In addition, the proposed technique provided high resolution pixel-by-pixel displacements among consecutive frames. On the contrary, kernel matching approaches entail sub-optimal resolution of displacement estimates, given that the approximate shift of a kernel consisting of multiple pixels is derived, compromising thus information on the exact pixel location of the displacing tissue. Furthermore, the employed neural network provided accurate displacement maps directly from the RF-signals, or B-mode images, without requiring additional processing steps such as cosine interpolation, sub-sampling displacements or low-pass filtering, which are often required in conventional displacement estimation techniques [58][65][66].

Training the model on the B-mode images provided higher elastographic signal-to-noise ratio, but lower contrast-to-noise ratio as compared to RF-frames. This can be due to the fact that given that the B-mode images include the log compressed envelope of the RF signals, which are expected to present smaller spatial variation and smoother delineation of arterial tissue, reducing thus the SNR. However, the uncompressed RF signals present higher variations in intensity, offering better contrast between moving tissue and background. Furthermore, using the RF-signals provided more accurate tracking of distension pulse wave propagation, as compared to B-mode images. Those results demonstrate the capability of RF signals to provide accurate information on the phase of the displacements, which may be more appropriate for applications involving wave propagation tracking at high temporal resolutions.

In the case of the in-vivo study, good agreement was found between the PWV values obtained through the deep learning-based and the conventional PWI methodologies. The deep learning displacement estimator provided more spatially homogeneous spatiotemporal maps and higher R^2, indicating improved quality of pulse wave tracking. This can be attributed to the fact that the trained neural network provides the pixel-by-pixel displacements among entire frames, enhancing spatial continuity of displacements estimated throughout the arterial walls. On the contrary, conventional PWI approach involves stitching displacements estimated from small kernels together, in order to form the displacement maps throughout the entire frames, which may deteriorate spatial continuity of wall displacements.

A limitation of this study arises from the fact that the developed technique was tested only in healthy straight vessel geometries. Atherosclerotic vessels may pose a challenge for the employed neural network to learn. In order to extend the technique to such vessels, a broader dataset, consisting of a mix of healthy and atherosclerotic vessels should be employed for the training process. In addition, pathological arteries with spatial variations in geometry

and mechanical properties may require adjustment of the regularization factor in the loss function, in order to prevent over-smoothing of the displacement field.

Future efforts involve training a more generalized model that can be inferred in different subjects without the need to retrain on specific datasets. Obtaining a model with good generalization capabilities is expected to significantly decrease the time needed for tissue displacement estimation, showing promise in real-time ultrasound elasticity imaging. A preliminary analysis involving comparison of the time efficiency of the presented deep learning method against a conventional motion tracking technique can be found in the Appendix.

Finally, the proposed displacement estimator was evaluated in terms of axial displacements. Given the restricted lateral resolution provided by the employed ultrasound setup, and the motion of the artery along the axial direction, performance assessment was carried out only in terms of axial displacements. Ongoing work includes assessing the capability of the proposed neural network to provide robust 2-D displacement maps.

5. Conclusion

In conclusion, an unsupervised deep learning-based approach was introduced for arterial wall displacement estimation. The proposed technique was evaluated in vessel phantom experiments and human common carotid arteries in-vivo, showing the feasibility to learn arterial motion patterns at high temporal and spatial resolutions. The developed method demonstrated the potential to address limitations entailed by conventional displacement estimators, improving thus the accuracy of vascular ultrasound elasticity imaging techniques.

Acknowledgement

This work was supported by a grant of the National Institutes of Health (NIH 1-R01-HL135734).

Appendix

Time efficiency is a significant benefit of the proposed deep learning-based displacement estimation technique. A comparison was carried out between the efficiency of the trained model and a conventional displacement estimator in terms of time (τ) taken to derive a 2-D displacement map between two consecutive temporal RF frames. The normalized cross-correlation technique described in [67] was applied on the filtered RF frames, to track arterial wall motion in 2-D. Selection of cross-correlation parameters was based on previous PWI implementation [58]. An axial kernel was shifted along the axial and lateral directions across adjacent RF frames, using a kernel shift of 1 axial sample (0.01848 mm). The size of the kernel was set at 7 axial samples (0.1293 mm). The maximum axial and lateral search range was set at 4 axial (0.0739 mm) and 1 lateral sample (0.298 mm), respectively. The time, τ, of the conventional cross-correlation method was equal to xx, which was xx times higher than the deep learning model.

References

[1]. Giudici A, Wilkinson IB, and Khir AW, “Review of the Techniques Used for Investigating the Role Elastin and Collagen Play in Arterial Wall Mechanics,” IEEE Rev. Biomed. Eng, vol. 14, pp. 256–269, 2021, doi: 10.1109/RBME.2020.3005448. [PubMed: 32746366]

[2]. Wagenseil JE and Mecham RP, “Elastin in large artery stiffness and hypertension,” J. Cardiovasc. Transl. Res, vol. 5, no. 3, pp. 264–273, jun. 2012, doi: 10.1007/S12265-012-9349-8/FIGURES/6. [PubMed: 22290157]

[3]. Bank AJ, Wang H, Holte JE, Mullen K, Shammas R, and Kubo SH, “Contribution of Collagen, Elastin, and Smooth Muscle to In Vivo Human Brachial Artery Wall Stress and Elastic Modulus,” Circulation, vol. 94, no. 12, pp. 3263–3270, Dec. 1996, doi: 10.1161/01.CIR.94.12.3263. [PubMed: 8989139]

[4]. Jani B and Rajkumar C, “Ageing and vascular ageing,” Postgrad. Med. J, vol. 82, no. 968, pp. 357–362, Jun. 2006, doi: 10.1136/PGMJ.2005.036053. [PubMed: 16754702]

[5]. Mattace-Raso FUS et al. . “Arterial Stiffness and Risk of Coronary Heart Disease and Stroke,” Circulation, vol. 113, no. 5, pp. 657–663, Feb. 2006, doi: 10.1161/CIRCULATIONAHA.105.555235. [PubMed: 16461838]

[6]. London GM and Safar ME, “Arterial wall remodelling and stiffness in hypertension: heterogeneous aspects.,” Clin. Exp. Pharmacol. Physiol, vol. 23, no. 8, pp. S1–5, Aug. 1996, doi: 10.1111/J.1440-1681.1996.TB03033.X. [PubMed: 8886505]

[7]. Grotta JC, “Carotid Stenosis,” N. Engl. J. Med, vol. 369, no. 12, pp. 1143–1150, Sep. 2013, doi: 10.1056/NEJMcpl214999. [PubMed: 24047063]

[8]. Apostolakis IZ, Nandlall SD, and Konofagou EE, “Piecewise Pulse Wave Imaging (pPWI) for Detection and Monitoring of Focal Vascular Disease in Murine Aortas and Carotids In Vivo,” IEEE Trans. Med. Imaging, vol. 35, no. 1, pp. 13–28, Jan. 2016, doi: 10.1109/TMI.2015.2453194. [PubMed: 26168432]

[9]. Apostolakis IZ, Karageorgos GM, Nauleau P, Nandlall SD, and Konofagou EE, “Adaptive Pulse Wave Imaging: automated spatial vessel wall inhomogeneity detection in phantoms and in-vivo,” IEEE Trans. Med. Imaging, pp. 1–1, 2019, doi:10.1109/TMI.2019.2926141.

[10]. Czernuszewicz TJ et al. , “Non-invasive in Vivo Characterization of Human Carotid Plaques with Acoustic Radiation Force Impulse Ultrasound: Comparison with Histology after Endarterectomy,” Ultrasound Med. Biol, vol. 41, no. 3, pp. 685–697, Mar. 2015, doi: 10.1016/J.ULTRASMEDBIO.2014.09.016. [PubMed: 25619778]

[11]. Lee RT et al. . “Prediction of mechanical properties of human atherosclerotic tissue by high-frequency intravascular ultrasound imaging. An in vitro study.,” Arterioscler. Thromb. A J. Vasc. Biol, vol. 12, no. 1, pp. 1–5. Jan. 1992, doi: 10.1161/01.ATV.12.1.1.

[12]. de Korte CL, Fekkes S, Nederveen AJ, Manniesing R, and Hansen HRHG, “Review: Mechanical Characterization of Carotid Arteries and Atherosclerotic Plaques,” IEEE Trans. Ultrason. Ferroelectr. Freq. Control, vol. 63, no. 10, pp. 1613–1623, Oct. 2016, doi: 10.1109/TUFFC.2016.2572260. [PubMed: 27249826]

[13]. Hansen HHG, de Borst GJ. Bots ML. Moll FL. Pasterkamp G, and de Korte CL, “Validation of Noninvasive In Vivo Compound Ultrasound Strain Imaging Using Histologic Plaque Vulnerability Features,” Stroke, vol. 47, no. 11, pp. 2770–2775, Nov. 2016, doi: 10.1161/STROKEAHA.116.014139. [PubMed: 27686104]

[14]. Hansen HHG, De Borst GJ, Bots ML, Moll F, Pasterkamp G, and De Korte CL, “Noninvasive compound ultrasound elastography for vulnerable plaque detection: in vivo validation,” Eur. Heart J, vol. 34, no. suppl 1, pp. P258–P258, Aug. 2013, doi: 10.1093/eurheartj/eht307.P258.

[15]. Roy Cardinal M-H et al. . “Carotid Artery Plaque Vulnerability Assessment Using Noninvasive Ultrasound Elastography: Validation With MRI,” Am. J. Roentgenol, vol. 209, no. 1, pp. 142–151, Jul. 2017, doi: 10.2214/AJR.16.17176. [PubMed: 28639927]

[16]. Dempsey RJ et al. . “Carotid atherosclerotic plaque instability and cognition determined by ultrasound-measured plaque strain in asymptomatic patients with significant stenosis,” J. Neurosurg, vol. 128, no. 1, pp. 111–119, Jan. 2018, doi: 10.3171/2016.10.JNS161299. [PubMed: 28298048]

[17]. Garrard J et al. . “Shear Wave Elastography May Be Superior to Greyscale Median for the Identification of Carotid Plaque Vulnerability: A Comparison with Histology,” Ultraschall der Medizin - Eur. J. Ultrasound, vol. 36, no. 04, pp. 386–390, Jun. 2015, doi: 10.1055/s-0034-1399676.

[18]. Ramnarine KV, Garrard JW, Kanber B, Nduwayo S, Hartshorne TC, and Robinson TG, “Shear wave elastography imaging of carotid plaques: feasible, reproducible and of clinical potential,” Cardiovasc. Ultrasound, vol. 12, no. 1, p. 49, Dec. 2014, doi: 10.1186/1476-7120-12-49. [PubMed: 25487290]

[19]. Widman E, Maksuti E, Larsson D, Urban MW, Bjällmark A, and Larsson M, “Shear wave elastography plaque characterization with mechanical testing validation: a phantom study,” Phys. Med. Biol, vol. 60, no. 8. pp. 3151–3174, Apr. 2015, doi: 10.1088/0031-9155/60/8/3151. [PubMed: 25803520]

[20]. Laurent S et al. , “Expert consensus document on arterial stiffness: methodological issues and clinical applications,” Eur. Heart. J, vol. 27, no. 21, pp. 2588–2605, Sep. 2006, doi: 10.1093/eurheartj/ehl254. [PubMed: 17000623]

[21]. van Popele NM et al. , “Association between arterial stiffness and atherosclerosis: the Rotterdam Study.,” Stroke, vol. 32, no. 2, pp. 454–60, Feb. 2001. [PubMed: 11157182]

[22]. Li RX, Luo J, Balaram SK, Chaudhry FA, Shahmirzadi D, and Konofagou EE, “Pulse wave imaging in normal, hypertensive and aneurysmal human aortas *in vivo* : a feasibility study,” Phys. Med Biol, vol. 58, no. 13, pp. 4549–4562, Jul. 2013, doi: 10.1088/0031-9155/58/13/4549. [PubMed: 23770991]

[23]. Fujikura K et al. , “A Novel Noninvasive Technique for Pulse-Wave Imaging and Characterization of Clinically-Significant Vascular Mechanical Properties *In Vivo*,” Ultrason. Imaging, vol. 29, no. 3, pp. 137–154, Jul. 2007, doi: 10.1177/016173460702900301. [PubMed: 18092671]

[24]. Nandlall SD, Goldklang MP, Kalashian A, Dangra NA, D’Armiento JM, and Konofagou EE, “Monitoring and staging abdominal aortic aneurysm disease with pulse wave imaging.,” Ultrasound Med. Biol, vol. 40, no. 10, pp. 2404–14, Oct. 2014, doi: 10.1016/j.ultrasmedbio.2014.04.013. [PubMed: 25130446]

[25]. Apostolakis I-Z, Nauleau P, Papadacci C, McGarry MD, and Konofagou EE, “Feasibility and Validation of 4-D Pulse Wave Imaging in Phantoms and In Vivo,” IEEE Trans. Ultrason. Ferroelectr. Freq. Control, vol. 64, no. 9, pp. 1305–1317, Sep. 2017, doi: 10.1109/TUFFC.2017.2735381. [PubMed: 28792891]

[26]. Nauleau P, Apostolakis I, McGarry M, and Konofagou E, “Cross-correlation analysis of pulse wave propagation in arteries: In vitro validation and in vivo feasibility,” Phys. Med Biol, vol. 63, no. 11, p. 115006, May 2018, doi: 10.1088/1361-6560/aabe57. [PubMed: 29658889]

[27]. Karageorgos GM et al. , “Imaging of pulse wave propagation coupled with vector flow and wall shear stress mapping in atherosclerotic plaque phantoms and in vivo,” IEEE Int. Ultrason. Symp. IUS, vol. 2019-October, pp. 243–246, Oct. 2019, doi: 10.1109/ULTSYM.2019.8925888.

[28]. Karageorgos GM, Apostolakis IZ, Nauleau P, Weber R, and Konofagou EE, “Automated Spatial Mechanical Inhomogeneity Detection and Arterial Wall Characterization in Human Atherosclerotic Carotid Arteries In-Vivo,” IEEE Int. Ultrason. Symp. IUS, vol. 2018-October, Dec. 2018, doi: 10.1109/ULTSYM.2018.8579974.

[29]. Karageorgos GM et al. , “Arterial wall mechanical inhomogeneity detection and atherosclerotic plaque characterization using high frame rate pulse wave imaging in carotid artery disease patients in vivo,” Phys. Med Biol, vol. 65, no. 2, p. 16, Jan. 2020, doi: 10.1088/136l-6560/ab58fa.

[30]. Li RX et al. , “Pulse Wave Imaging in Carotid Artery Stenosis Human Patients in Vivo.,” Ultrasound Med. Biol, vol. 0, no. 0, Nov. 2018, doi: 10.1016/j.ultrasmedbio.2018.07.013.

[31]. Karageorgos GM, Apostolakis IZ, Nauleau P, Gatti V, Weber R, and Konofagou EE, “Atherosclerotic plaque mechanical characterization coupled with vector Doppler imaging in atherosclerotic carotid arteries in-vivo,” in Proceedings of the Annual International Conference of the IEEE Engineering in Medicine and Biology Society, EMBS, 2019, pp. 6200–6203, doi:10.1109/EMBC.2019.8857609.

[32]. Gami P, Kemper P, Karageorgos G, Swingle T, Webber R, and Konofagou EE, “Characterization of Nonlinear Elasticity of the Carotid Artery Using Pulse Wave Imaging: a Feasibility Study in

Hypertensive and Carotid Artery Disease Patients in Vivo," IEEE Int. Ultrason. Symp. IUS, vol. 2022-October, 2022, doi:10.1109/IUS54386.2022.9957838.

[33]. Kemper P et al. , "Physiological Measurement Feasibility of longitudinal monitoring of atherosclerosis with pulse wave imaging in a swine model You may also like Feasibility of longitudinal monitoring of atherosclerosis with pulse wave imaging in a swine model," Physiol. Meas, vol. 42, p. 105008, 2021, doi: 10.1088/1361-6579/ac290f.

[34]. Karageorgos GM et al. , "Adaptive Wall Shear Stress Imaging in Phantoms, Simulations and in Vivo," IEEE Trans. Biomed. Eng, vol. 70, no. 1, pp. 154–165, Jan. 2023, doi: 10.1109/TBME.2022.3186854. [PubMed: 35776824]

[35]. Luo J and Konofagou E, "A fast normalized cross-correlation calculation method for motion estimation," IEEE Trans. Ultrason. Ferroelectr. Freq. Control, vol. 57, no. 6, pp. 1347–1357, Jun. 2010, doi: 10.1109/TUFFC.2010.1554. [PubMed: 20529710]

[36]. Poree J, Garcia D, Chayer B, Ohayon J, and Cloutier G, "Noninvasive Vascular Elastography With Plane Strain Incompressibility Assumption Using Ultrafast Coherent Compound Plane Wave Imaging," IEEE Trans. Med. Imaging, vol. 34, no. 12, pp. 2618–2631, Dec. 2015, doi: 10.1109/TMI.2015.2450992. [PubMed: 26625341]

[37]. Luo Jianwen, Fujikura K, Tyrie LS, Tilson MD, and Konofagou EE, "Pulse Wave Imaging of Normal and Aneurysmal Abdominal Aortas In Vivo," IEEE Trans. Med. Imaging, vol. 28, no. 4, pp. 477–486, Apr. 2009, doi: 10.1109/TMI.2008.928179. [PubMed: 19272985]

[38]. Hansen H, Lopata R, and de Korte CL, "Noninvasive Carotid Strain Imaging Using Angular Compounding at Large Beam Steered Angles: Validation in Vessel Phantoms," IEEE Trans. Med. Imaging, vol. 28, no. 6, pp. 872–880, Jun. 2009, doi: 10.1109/TMI.2008.2011510. [PubMed: 19131297]

[39]. McDicken WN, Sutherland GR, Moran CM, and Gordon LN, "Colour doppler velocity imaging of the myocardium," Ultrasound Med. Biol, vol. 18, no. 6–7, pp. 651–654, Jan. 1992, doi: 10.1016/030l-5629(92)90080-T. [PubMed: 1413277]

[40]. Poree J, Posada D, Hodzic A, Tournoux F, Cloutier G, and Garcia D, "High-Frame-Rate Echocardiography Using Coherent Compounding with Doppler-Based Motion-Compensation," IEEE Trans. Med Imaging, vol. 35, no. 7, pp. 1647–1657, Jul. 2016, doi: 10.1109/TMI.2016.2523346. [PubMed: 26863650]

[41]. Eriksson A, Greiff E, Loupas T, Persson M, and Pesque P, "Arterial pulse wave velocity with tissue doppler imaging," Ultrasound Med. Biol, vol. 28, no. 5, pp. 571–580, May 2002, doi: 10.1016/S0301-5629(02)00495-7. [PubMed: 12079694]

[42]. Schmidt-Trucksäss A et al. , "Assessment of carotid wall motion and stiffness with tissue doppler imaging," Ultrasound Med. Biol, vol. 24, no. 5, pp. 639–646, Jun. 1998, doi: 10.1016/S0301-5629(98)00023-4. [PubMed: 9695266]

[43]. Jia C et al. , "Comparison of 2-D speckle tracking and tissue Doppler imaging in an isolated rabbit heart model," IEEE Trans. Ultrason. Ferroelectr. Freq. Control, vol. 57, no. 11, pp. 2491–2502, Nov. 2010, doi: 10.1109/TUFFC.2010.1715. [PubMed: 21041136]

[44]. Sun D, Yang X, Liu MY, and Kautz J, "PWC-Net: CNNs for Optical Flow Using Pyramid, Warping, and Cost Volume," Proc. IEEE Comput. Soc. Conf. Comput. Vis. Pattern Recognit, pp. 8934–8943, Sep. 2017, doi: 10.1109/CVPR.2018.00931.

[45]. Peng B, Xian Y, Zhang Q, and Jiang J, "Neural-network-based Motion Tracking for Breast Ultrasound Strain Elastography: An Initial Assessment of Performance and Feasibility," Ultrason. Imaging, vol. 42, no. 2, pp. 74–91, Mar. 2020, doi: 10.1177/0161734620902527/FORMAT/EPUB. [PubMed: 31997720]

[46]. Tehrani AKZ and Rivaz H, "Displacement Estimation in Ultrasound Elastography Using Pyramidal Convolutional Neural Network," IEEE Trans. Ultrason. Ferroelectr. Freq. Control, vol. 67, no. 12, pp. 2629–2639, Dec. 2020, doi: 10.1109/TUFFC.2020.2973047. [PubMed: 32070949]

[47]. Chan DY, Morris DC, Polascik TJ, Palmeri ML, and Nightingale KR, "Deep Convolutional Neural Networks for Displacement Estimation in ARFI Imaging," IEEE Trans. Ultrason. Ferroelectr. Freq. Control, vol. 68, no. 7, pp. 2472–2481, Jul. 2021, doi: 10.1109/TUFFC.2021.3068377. [PubMed: 33760733]

[48]. Xiao C et al. , “A new deep learning method for displacement tracking from ultrasound RF signals of vascular walls,” Comput. Med. Imaging Graph, vol. 87, p. 101819, Jan. 2021, doi: 10.1016/J.COMPMEDIMAG.2020.101819. [PubMed: 33341465]

[49]. Tehrani AKZ, Mirzaei M, and Rivaz H, “Semi-supervised Training of Optical Flow Convolutional Neural Networks in Ultrasound Elastography,” Lect. Notes Comput. Sci. (including Subser. Lect. Notes Artif. Intell. Lect. Notes Bioinformatics), vol. 12263 LNCS, pp. 504–513, 2020, doi: 10.1007/978-3-030-59716-048/COVER.

[50]. Delaunay R, Hu Y, and Vercauteren T, “An unsupervised learning approach to ultrasound strain elastography with spatio-temporal consistency,” Phys. Med. Biol, vol. 66, no. 17, Sep. 2021, doi: 10.1088/1361-6560/AC176A.

[51]. Delaunay R, Hu Y, and Vercauteren T, “An Unsupervised Approach to Ultrasound Elastography with End-to-end Strain Regularisation,” Lect. Notes Comput. Sci. (including Subser. Lect. Notes Artif. Intell. Lect. Notes Bioinformatics), vol. 12263 LNCS, pp. 573–582, 2020, doi: 10.1007/978-3-030-59716-055/COVER.

[52]. Ahn SS, Ta K, Lu A, Stendahl JC, Sinusas AJ, and Duncan JS, “Unsupervised motion tracking of left ventricle in echocardiography,” 10.1117/12.2549572, vol. 11319, pp. 196–202, Mar. 2020, doi: 10.1117/12.2549572.

[53]. Ta K, Ahn SS, Lu A, Stendahl JC, Sinusas AJ, and Duncan JS, “A Semi-Supervised Joint Learning Approach to Left Ventricular Segmentation and Motion Tracking in Echocardiography,” Proc. - Int. Symp. Biomed. Imaging, vol. 2020-April, pp. 1734–1737, Apr. 2020, doi: 10.1109/ISBI45749.2020.9098664.

[54]. Balakrishnan G, Zhao A, Sabuncu MR, Guttag J, and Dalca AV, “VoxelMorph: A Learning Framework for Deformable Medical Image Registration,” IEEE Trans. Med. Imaging, vol. 38, no. 8, pp. 1788–1800, Aug. 2019, doi: 10.1109/TMI.2019.2897538.

[55]. Vittorio G, Nauleau P, Karageorgos GM, Shim J, Ateshian G, and Konofagou E, “Modelling pulse wave propagation through a stenotic artery with fluid structure interaction: a validation study using ultrasound pulse wave imaging,” Biomech. Model. Mechanobiol

[56]. Karageorgos GM et al. , “Pulse wave imaging coupled with vector flow mapping: A phantom, simulation and in vivo study,” IEEE Trans. Ultrason. Ferroelectr. Freq. Control, pp. 1–1, 2021, doi: 10.1109/TUFFC.2021.3074113.

[57]. Mobadersany N et al. , “Pulse wave imaging of a stenotic artery model with plaque constituents of different stiffnesses: Experimental demonstration in phantoms and fluid-structure interaction simulation,” J. Biomech, vol. 149, Mar. 2023, doi: 10.1016/J.JBIOMECH.2023.111502.

[58]. Apostolakis IZ, McGarry MDJ, Bunting EA, and Konofagou EE, “Pulse wave imaging using coherent compounding in a phantom and *in vivo*,” Phys. Med. Biol, vol. 62, no. 5, pp. 1700–1730, Mar. 2017, doi: 10.1088/1361-6560/aa553a. [PubMed: 28002039]

[59]. Ronneberger O, Fischer P, and Brox T, “U-Net: Convolutional Networks for Biomedical Image Segmentation,” Lect. Notes Comput. Sci. (including Subser. Lect. Notes Artif. Intell. Lect. Notes Bioinformatics), vol. 9351, pp. 234–241, 2015, doi: 10.1007/978-3-319-24574-4_28.

[60]. Avants BB, Epstein CL, Grossman M, and Gee JC, “Symmetric diffeomorphic image registration with cross-correlation: Evaluating automated labeling of elderly and neurodegenerative brain,” Med. Image Anal, vol. 12, no. 1, pp. 26–41, Feb. 2008, doi: 10.1016/J.MEDIA.2007.06.004. [PubMed: 17659998]

[61]. “GitHub - keras-team/keras: Deep Learning for humans.” [Online]. Available: https://github.com/keras-team/keras. [Accessed: 07-Feb-2022].

[62]. Abadi M et al., “TensorFlow: Large-Scale Machine Learning on Heterogeneous Distributed Systems.”

[63]. Santhiyakumari N, Madheswaran M, and Madheswaran M, “Noninvasive evaluation of carotid artery wall thickness using improved dynamic programming technique,” SIViP, vol. 2, pp. 183–193, 2008, doi: 10.1007/s11760-007-0048-x.

[64]. Varghese T and Ophir J, “An analysis of elastographic contrast-to-noise ratio,” Ultrasound Med. Biol, vol. 24, no. 6, pp. 915–924, Jul. 1998, doi: 10.1016/S0301-5629(98)00047-7. [PubMed: 9740393]

[65]. Azar RZ, Goksel O, and Salcudean SE, “Sub-sample displacement estimation from digitized ultrasound RF signals using multi-dimensional polynomial fitting of the cross-correlation function.” IEEE Trans. Ultrason. Ferroelectr. Freq. Control, vol. 57, no. 11, pp. 2403–2420, Nov. 2010, doi: 10.1109/TUFFC.2010.1708. [PubMed: 21041129]

[66]. McCormick MM and Varghese T, “An approach to unbiased subsample interpolation for motion tracking,” Ultrason. Imaging, vol. 35, no. 2, pp. 76–89, Mar. 2013, doi: 10.1177/0161734613476176. [PubMed: 23493609]

[67]. Konofagou E and Ophir J, “A new elastographic method for estimation and imaging of lateral displacements, lateral strains, corrected axial strains and Poisson’s ratios in tissues,” Ultrasound Med. Biol, vol. 24, no. 8, pp. 1183–1199, Oct. 1998, doi: 10.1016/S0301-5629(98)00109-4. [PubMed: 9833588]

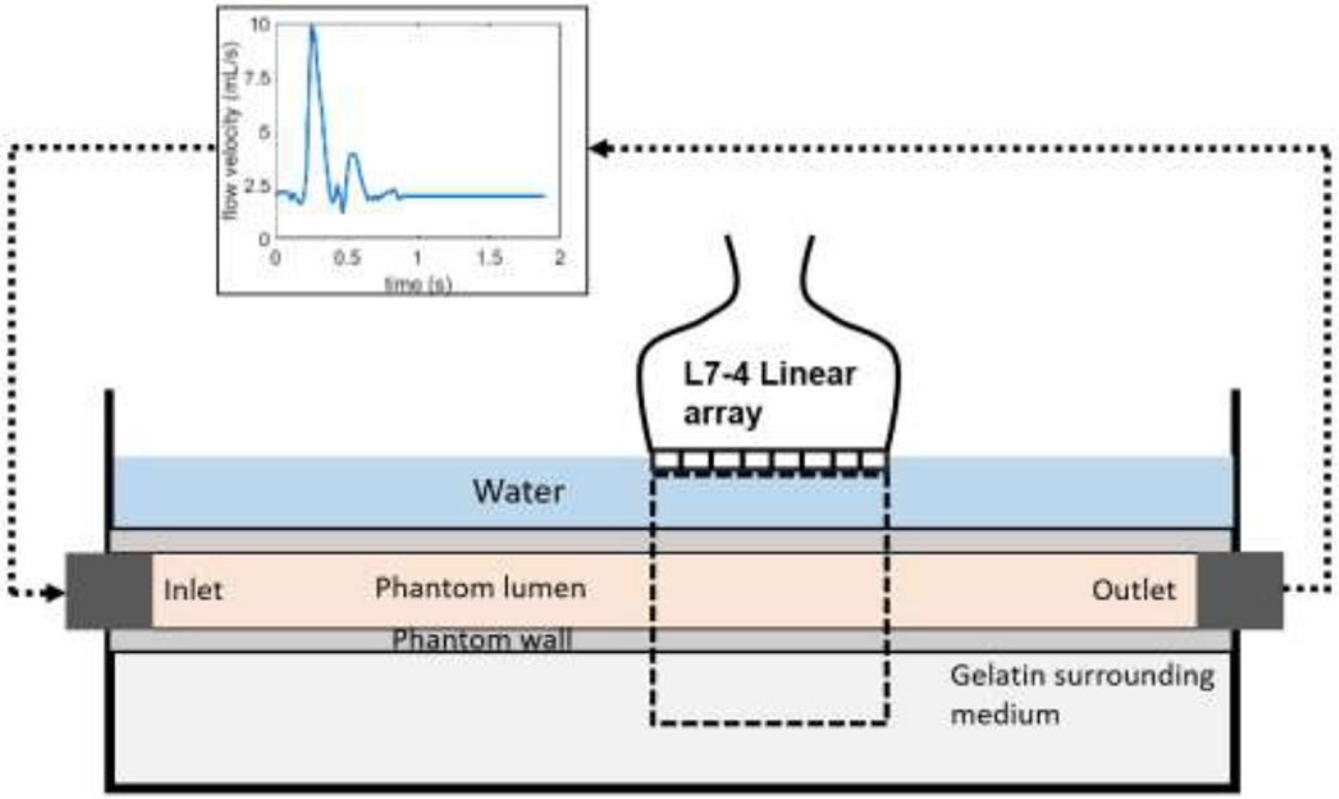

Figure 1:
Vessel phantom experimental setup. A straight vessel phantom is attached onto two plastic fittings in a plastic container and embedded in gelatin surrounding medium. A programmable pump applies a pulsatile flow waveform in the phantom lumen, and a linear array transducer is fixed on top of the container to acquire ultrasound RF data.

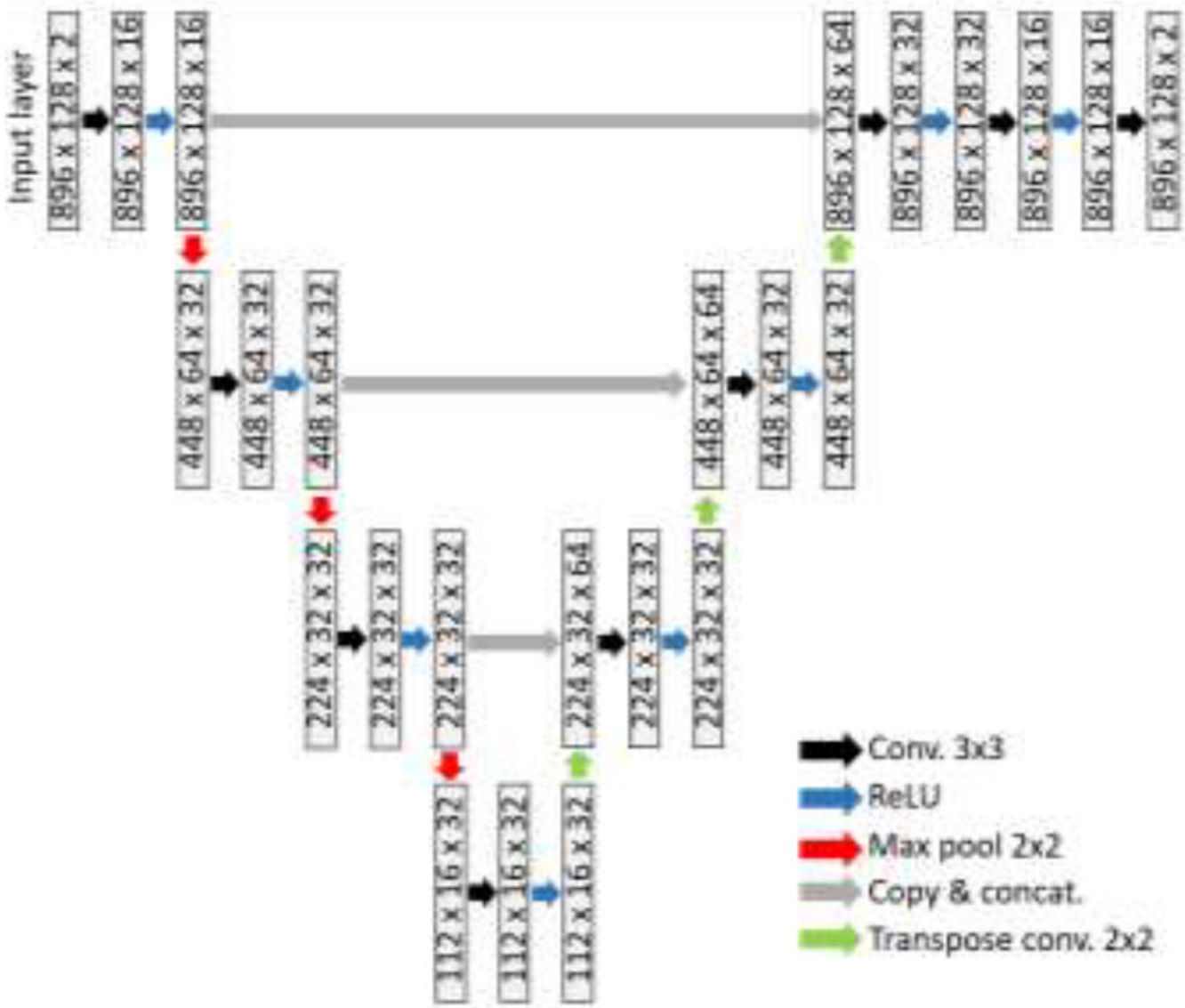

Figure 2:

U-net architecture used to transform a pair of consecutive temporal ultrasound frames to a displacement field. The numbers inside the gray rectangles denote the dimensions of the feature maps at each layer of the encoding and decoding stages.

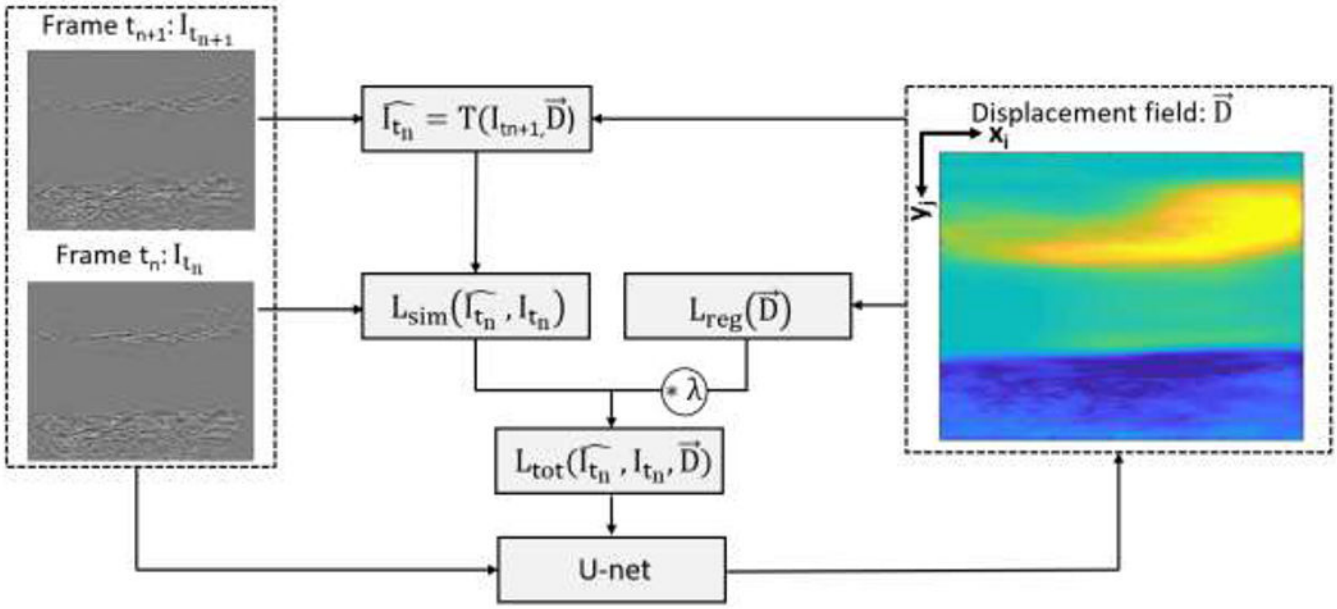

Figure 3:

Unsupervised deep learning approach for ultrasound image spatial registration. A pair of consecutive temporal ultrasound images, (I_{t_n}, $I_{t_{n+1}}$), are fed to a U-net, which applies appropriate transformations to derive the displacement field, $\vec{D}$. $\vec{D}$ is subsequently used to move temporal frame $I_{t_{n+1}}$ using a transformation T(), in order to approximate the frame I_{t_n}. Appropriate loss functions are calculated to evaluate the similarity between the generated image and the original I_{t_n}.

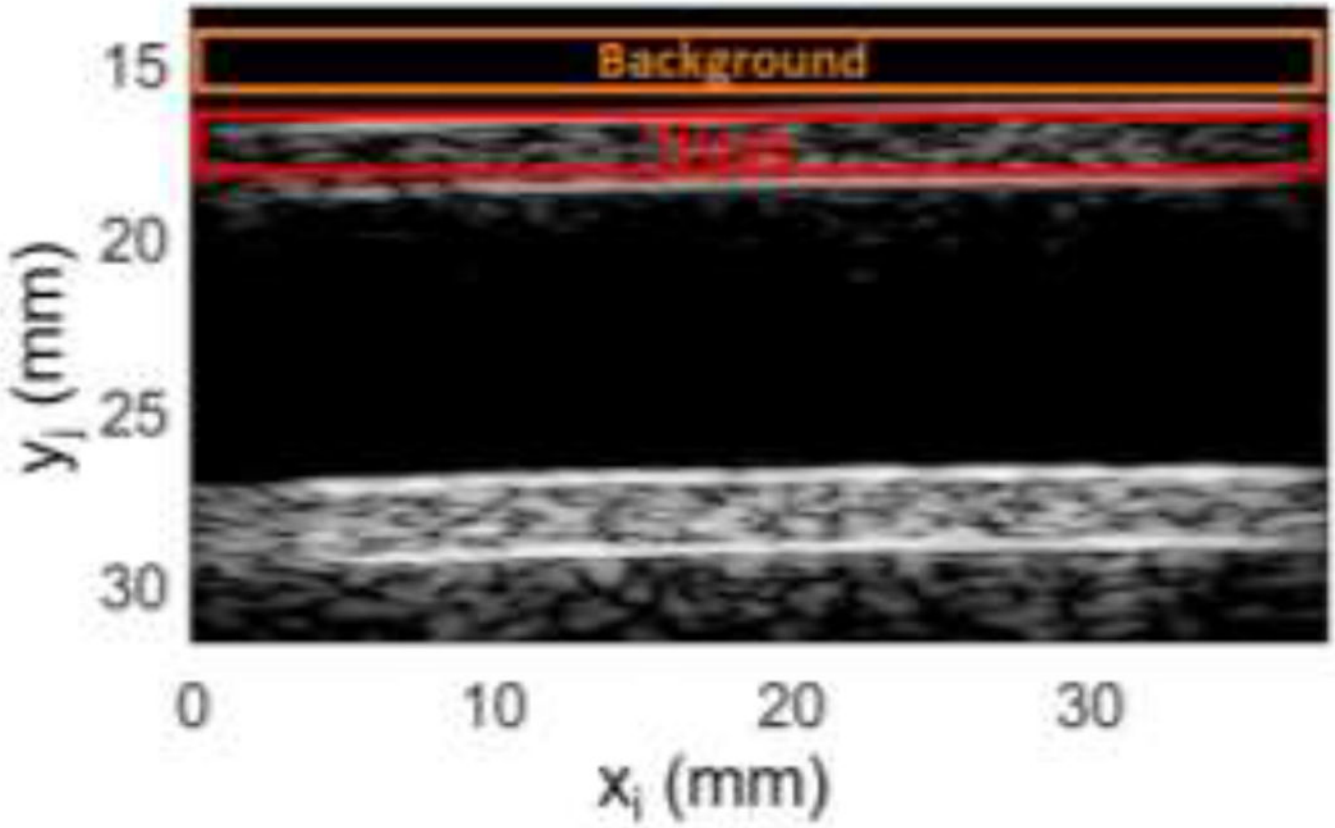

Figure 4:
Inclusions corresponding to Tissue and Background, for elastographic contrast-to-noise ratio (CNE_e) calculation.

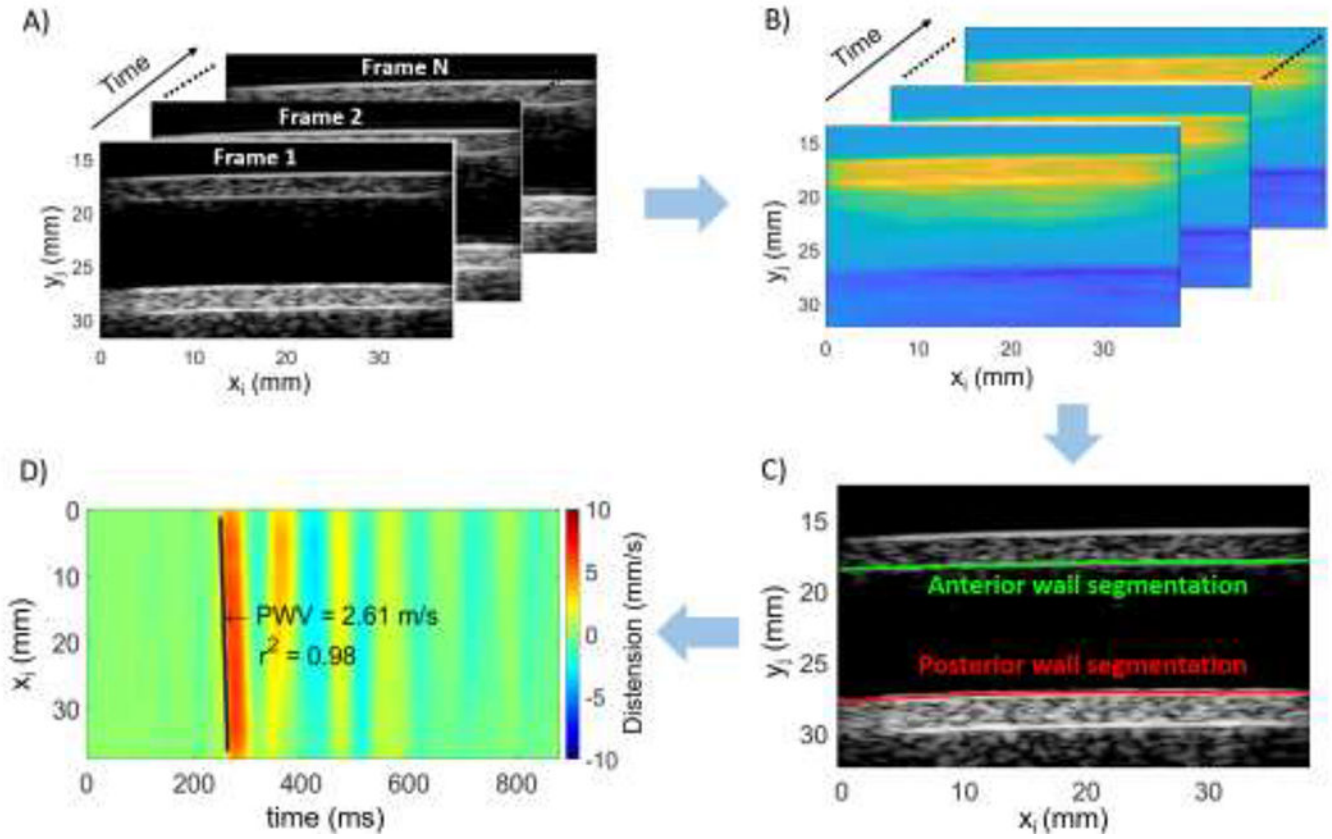

Figure 5:

Adjusted pulse wave imaging (PWI) processing methodology with the deep learning-based displacement estimator. A) Stack of consecutive temporal ultrasound frames. B) Displacement maps depicting the motion of each point location in the stack of temporal ultrasound frames. C) Manual wall segmentation of the proximal and distal wall of the vessel phantom. D) Spatiotemporal plot of phantom distension expressed in terms of velocities. A fit is applied to track the propagation of the distension pulse wave to estimate the PWV and the R^2.

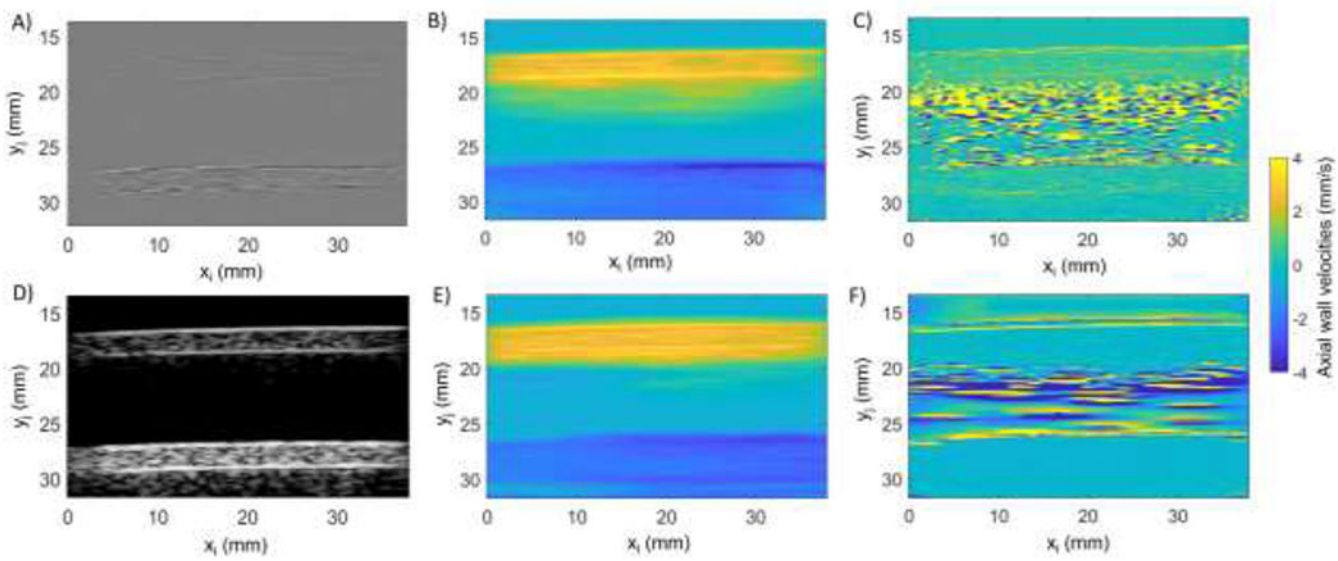

Figure 6:

A) Example RF frame from the validation dataset. B),C) Axial velocity maps resulting from the model trained on RF frames by using the MSE and NCC loss functions, respectively. D) B-mode image corresponding to the RF frame in Figure 6–A), E),F) Respective velocities using the model trained on the B-mode images (MSE, NCC, respectively).

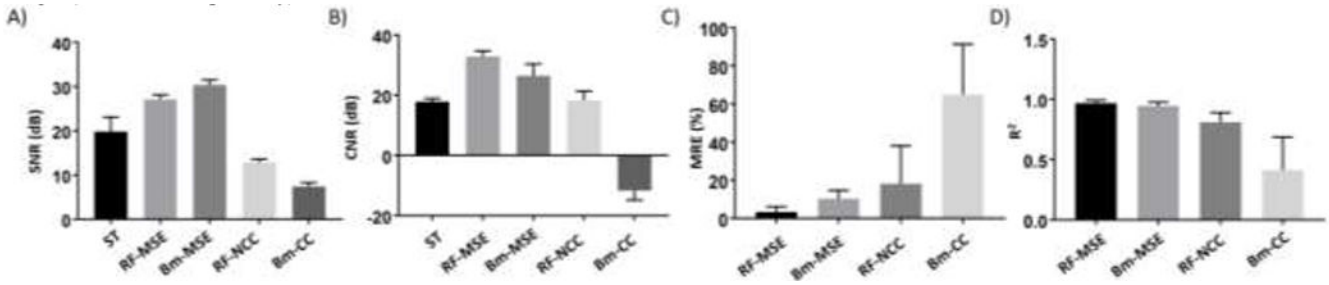

Figure 7:

A),B) Average and standard deviation of the SNR_e and CNR_e values, respectively, obtained by each trained model and the reference conventional displacement estimator. C,D) Average and standard deviation of MRE_{PWV} and R^2, respectively, obtained by each trained model.

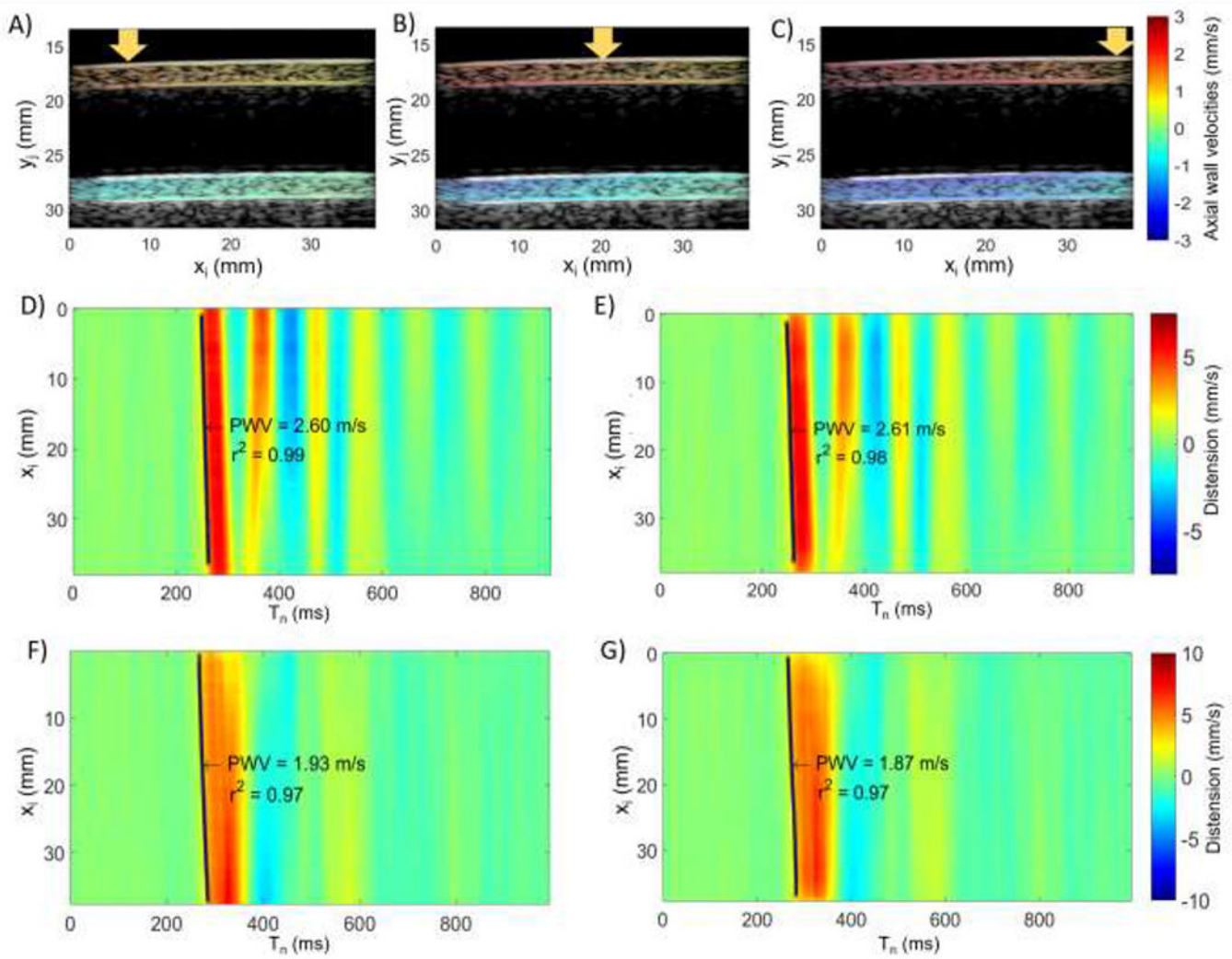

Figure 8:

A-C) Time frames of the PWI image sequence derived through the RF-MSE model, in a phantom validation acquisition. The axial wall velocities are color-coded and overlaid onto the B-mode image. The yellow arrow indicates the position of the wave-front of the pulse wave at each given time-frame. D, E) demonstrate the spatiotemporal map of arterial wall distension, as obtained through conventional PWI and RF-MSE in an example validation acquisition. F, G) show the respective PWI and RF-MSE spatiotemporal maps in an example test acquisition.

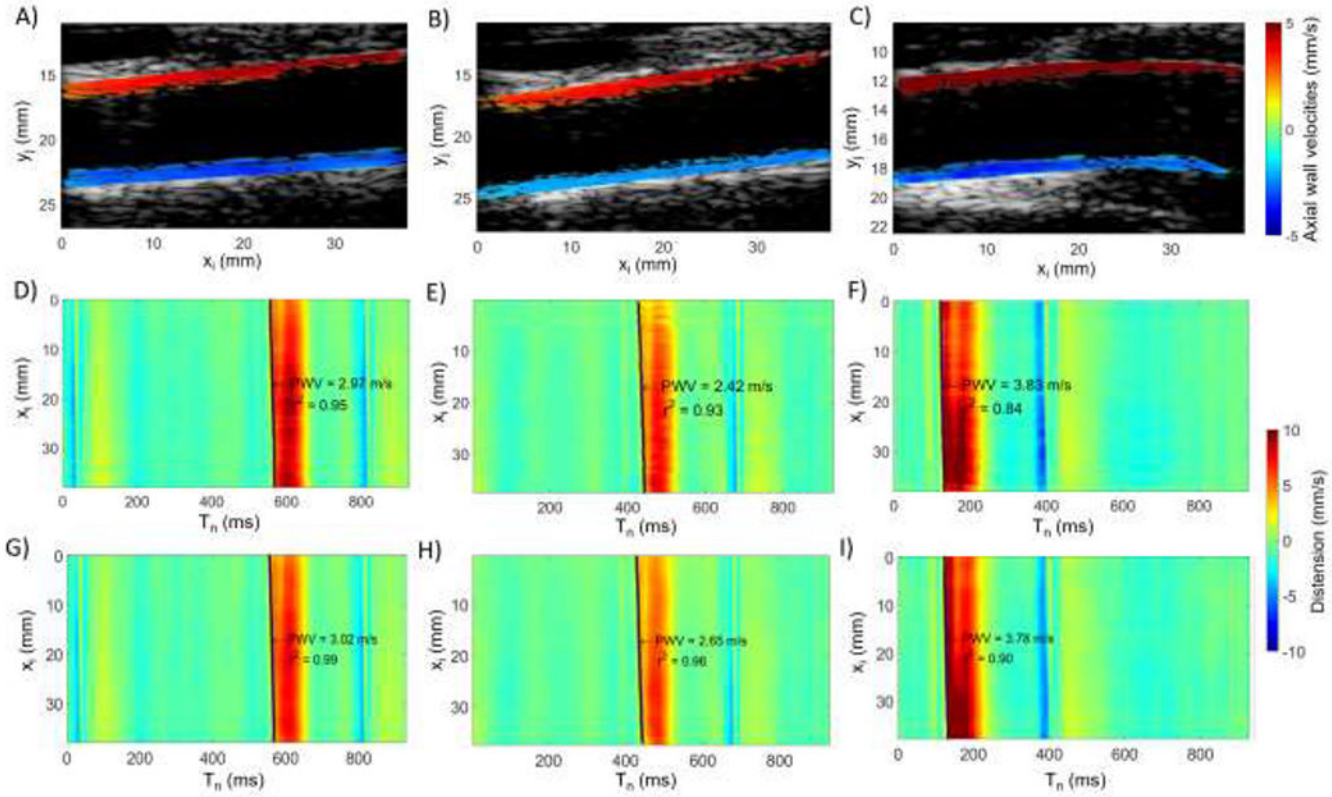

Figure 9:

A-C) Three in-vivo examples of the validation dataset. The axial wall velocities derived through RF-MSE are color-coded and overlaid onto the B-mode image. D-F) Spatiotemporal maps, along with the estimated PWV and R^2 as obtained through conventional PWI, corresponding to images shown in A-C), respectively. G-I) Respective spatiotemporal maps, as obtained through the RF-MSE model.

TABLE I:

Summary of test phantom PWV and R^2 values

	Conventional PWI		RF-MSE	
# acquisition	**PWV (m/s)**	**R^2**	**PWV (m/s)**	**R^2**
1	2.21	0.99	2.33	0.98
2	2.58	0.98	2.6	0.98
3	2.26	0.99	2.22	0.99
4	2.37	0.99	2.41	0.98
5	1.87	0.97	1.93	0.97

TABLE II:

Summary of in-vivo PWV and R^2 values

	Conventional PWI		RF-MSE	
# acquisition	**PWV (m/s)**	**R^2**	**PWV (m/s)**	**R^2**
1	2.42	0.93	2.65	0.96
2	2.97	0.95	3.02	0.99
3	3.83	0.84	3.78	0.9
4	0.57	0.97	3.7	0.98
5	3.65	0.95	3.79	0.95
6	4.69	0.92	4.54	0.94